nature communications

Article

https://doi.org/10.1038/s41467-026-74365-6

Designing effective single-molecule electromagnets with radially π-conjugated carbon structures

Received: 1 October 2025

Accepted: 5 June 2026

Published online: 11 June 2026

Check for updates

Wanzhuo Shi [1,2], Richard Korytár [3], Ferdinand Evers [3,4], John D. Tovar [5,6] & Latha Venkataraman [1,2,7]

When charge flows through a molecular circuit, it induces a magnetic field that allows the circuit to behave as a nanoscale electromagnet. However, in single-molecule circuits this magnetic field is usually weak. Here we show that radially π-conjugated carbon structures can support amplified circulating currents that generate local magnetic fields. Within tight-binding and density functional theory (DFT) frameworks, we first study cycloparaphenylene (CPP) junctions where both electrodes are attached to the same phenylene unit on the nanohoop. We observe an energy-dependent ring current component that traverses the whole macrocycle by mapping the local current density. Importantly, we find that destructive interference near degenerate resonances can reverse the ring current direction and amplify it strongly relative to the source–drain current. We show that this interference-driven design principle is general, and also carries over to C_{60} junctions. In fullerene, lower-lying degenerate resonances are more easily accessible through electrostatic gating, reaching a magnetic field of 14.2 mT under a 100 mV source–drain bias. This work thus provides new insights into ring currents in radially π-conjugated carbon structures and highlights their potential as design platforms for single-molecule electromagnets.

When current flows through a macroscopic loop, it produces an axial magnetic field that is given by the Biot–Savart law. The same law holds for ballistic charge transport at the single-molecule scale. Yet in single-molecule junctions, the magnetic field is usually very small and in the microtesla (μT) range[1]. One intuitive route to increase the magnitude of this field is to simply shrink the diameter of the molecular loop, since the field strength is inversely proportional to loop diameter[2]. However, this strategy is also not ideal; the ring size cannot be infinitely small, and the attainable magnetic dipole moment ($m = I \times A$) is limited due to the reduced loop area. Another approach is to boost the current through the loop. While the conductance across a single-channel is restricted to $G_0 = 2e^2/h$, limiting the junction current, the local current distribution in a multipath structure can be larger[3]. Therefore, a single-molecule junction can sustain a ring current that far exceeds the net source–drain current[1,4,5]. Engineering an amplified ring current in a single-molecule macrocycle could therefore lead to a magnetic field that is significant across a relatively large area.

Molecules with radial π-conjugation include 2D rings such as cycloparaphenylenes (CPPs) and 3D spheres such as fullerenes. CPPs are carbon nanohoops in which benzene rings are joined at their para positions to create radially conjugated, cyclic macrocycles[6]. Since 2008[7], synthesis of CPPs has expanded to small, highly strained rings

[1]Department of Chemistry, Columbia University, New York, NY, USA. [2]Institute of Science and Technology Austria, Klosterneuburg, Austria. [3]Institute of Theoretical Physics, University of Regensburg, Regensburg, Germany. [4]Halle-Berlin-Regensburg Cluster of Excellence CCE, Regensburg, Germany. [5]Department of Chemistry, Johns Hopkins University, Baltimore, MD, USA. [6]Department of Materials Science and Engineering, Johns Hopkins University, Baltimore, MD, USA. [7]Department of Applied Physics and Applied Mathematics, Columbia University, New York, NY, USA.
e-mail: latha.venkataraman@ist.ac.at

such as [5]CPP and to gram-scale quantities, enabling systematic size-property studies[8–14]. Their unique curved π-systems and radial conjugation yield strong, predictable trends in electronic structure and optical properties, including size-dependent gaps between the highest occupied molecular orbital (HOMO) and the lowest unoccupied molecular orbital (LUMO) and bright, tunable emission[15–17]. Fullerenes provide a 3D realization of radial π-conjugation. In particular, C_{60} is a prototypical fullerene with a highly symmetric cage and low-lying electron-accepting states[18,19]. Together, CPPs and fullerenes offer closed, radially π-conjugated carbon networks in which bias-driven circulating currents may be amplified by quantum interference.

At the single-molecule level, previous studies have shown that radial π-conjugation modulates conductance in ways distinct from linear oligoparaphenylenes, yet nearly all prior transport measurements have probed current across the hoop between diametrically opposed sites[20–22]. Conductance through C_{60}-based molecular junctions has also been measured[23,24], and gate-controlled charge transport has been demonstrated in single-C_{60} transistor devices[25]. It remains unexplored whether radially π-conjugated carbon structures can be engineered to sustain circulating currents strong enough to generate experimentally relevant local magnetic fields.

Here, we provide design principles for single-molecule electromagnets, i.e., a single-molecule device whose bias-driven current density contains a net circulating component, with calculated magnetic fields that can exceed established nanoscale magnetometry detection thresholds at nanometer standoff distances. We first present calculations using CPPs as prototypical radially π-conjugated systems and then illustrate that the same principles apply to C_{60}-based molecular junctions. We use a nearest-neighbor tight-binding model to illustrate the basic principles and then carry out DFT electronic structure calculations with nonequilibrium Green's function (NEGF) method to analyze charge transport, ring currents, and magnetic response. The two electrodes are attached to the molecule, and we decompose the net source–drain transmission into local current density maps, exposing a nonzero ring current component that circulates around the CPP and quantifying how its magnitude depends on CPP size and energy. We find that delocalized frontier orbitals amplify the circulating component, whereas states localized on the contact phenylene dominate the net current while contributing essentially zero to the ring current. Interestingly, near doubly degenerate resonances that interfere destructively, we observe an energy-dependent reversal of the ring current direction along with a large increase in its magnitude. Through electrostatic gating, we show that it becomes possible to switch the direction of the ring current and enhance its magnitude strongly relative to the net current. Finally, we show that the same interference-driven design principle also applies to single-C_{60} junctions, where a 14.2 mT can be generated with a source–drain bias of 100 mV.

Results

Orbital structure of cycloparaphenylenes

To elucidate charge transport of π-conjugated CPPs, we start with a Hückel (tight-binding) model to understand the physical impacts of structure on transmission and ring currents. In this model, each carbon atom in the conjugated structure contributes a single p_z orbital with on-site energy ε. Since all carbon atoms are chemically equivalent, we set $\varepsilon = 0$ for simplicity and without loss of generality. Interactions between neighboring atomic sites are represented by the hopping integral t, and only nearest-neighbor interactions are considered. Following this approach, the Hamiltonian matrix for an isolated CPP structure can be expressed as:

$$H_{CPP} = -t\sum_{p=1}^{n}\sum_{q=1}^{6}|p,q\rangle\langle p,(q \bmod 6)+1| - t\sum_{p=1}^{n}|p,4\rangle\langle(p \bmod n)+1,1| + H.C. \quad (1)$$

Here, n represents the number of phenylene units within the ring, and the indices (p, q) denote the atomic site q in phenylene p. The first term represents the bonds that define each individual phenylene unit, while the second term connects ring p to ring $p+1$ through para positions, closing the conjugated macrocycle.

At the single-molecule scale, charge transport is coherent, and electrons tunnel through the bridge ballistically via discrete molecular orbitals[26]. We therefore begin by analyzing the orbitals of an isolated [n]CPP (Fig. 1a). Since the molecule is a periodic chain of identical phenylene units, we first treat an infinite CPP and work in k-space. The Bloch Hamiltonian is

$$H(k) = -t(\sum_{q=1}^{6}|q\rangle\langle(q \bmod 6)+1| + H.c.) - t(|4\rangle\langle 1|e^{ika} + |1\rangle\langle 4|e^{-ika}) \quad (2)$$

where the phase factors, $e^{\pm ika}$, arise directly from the Bloch's theorem. Diagonalizing $H(k)$ yields the electronic band structure of the infinite polymer shown in Fig. 1b:

$$E_{1,2,3,4}(k) = \pm t\sqrt{3 \pm 2\sqrt{2}\cos(ka/2)}, E_{5,6}(k) = \pm t \quad (3)$$

To obtain the molecular orbitals of a finite [n]CPP molecule, a cyclic boundary condition is imposed on the system that implies the following selection rules:

$$kna = 2\pi m; m \in Z \quad (4)$$

they restrict the wavevector to a discrete set, i.e., $k_m = 2\pi m/na$, that satisfies the cyclic symmetry of the [n]CPP molecule.

Taking [5]CPP as an example, five k values, i.e., $0, \pm 2\pi/5a, \pm 4\pi/5a$, are allowed within the first Brillouin zone, generating 30 discrete eigenvalues, as illustrated in Fig. 1b. The corresponding wavefunctions are also calculated (four samples are shown in Fig. 1c–f and the others in Supplementary Fig. 1; see also Supplementary Note 1). The LUMO and HOMO are non-degenerate with energies $E = \pm\left(\sqrt{2}-1\right)t$. The energies of these frontier orbitals are size-independent because the wavevector $k = 0$ always satisfies the cyclic boundary condition. Their wavefunctions are uniformly delocalized along the whole CPP cycle and have the same phase on every ring accordingly (Fig. 1c, d). It is worth noting, however, that experimentally the HOMO–LUMO gap of [n]CPPs increases modestly with ring size, a trend our highly simplified tight-binding model misses because it neglects factors such as strain and the torsional twist between adjacent phenylene rings, etc.[27–29]. In contrast, the bands at $E = \pm t$ are perfectly flat, indicating localized states. For [5]CPP, the orbitals related to these flat bands are five-fold degenerate and only the orbital with amplitude on the ring contacted to the electrodes is displayed (Fig. 1e, f), as this state contributes to the transmission. The remaining degenerate orbitals are provided in Supplementary Fig. 1. Except for the $k = 0$ and the flat-band orbitals, the others are all doubly degenerate, owing to the $\pm k$ pairs as a result of the cyclic boundary conditions and the band structure symmetry $E(k) = E(-k)$. Figure 1g, h shows examples of such doubly degenerate states, where the wavefunction amplitudes alternate in sign around the CPP ring.

Charge transport through cycloparaphenylene junctions

To model a single-molecule junction, the CPP needs to be contacted at the source (S) and drain (D) electrodes. The para connection pattern breaks the mirror symmetry of the isolated CPP (Fig. 1a). The electrode couplings break the mirror symmetry since the carbon atoms linked to the S and D leads are no longer equivalent to the others, resulting in a handedness to the junction. In other words, the electronic structure of the single-molecule junction becomes chiral even though the bare CPP molecule is not. When this mirror symmetry is broken, a net clockwise

https://doi.org/10.1038/s41467-026-74365-6

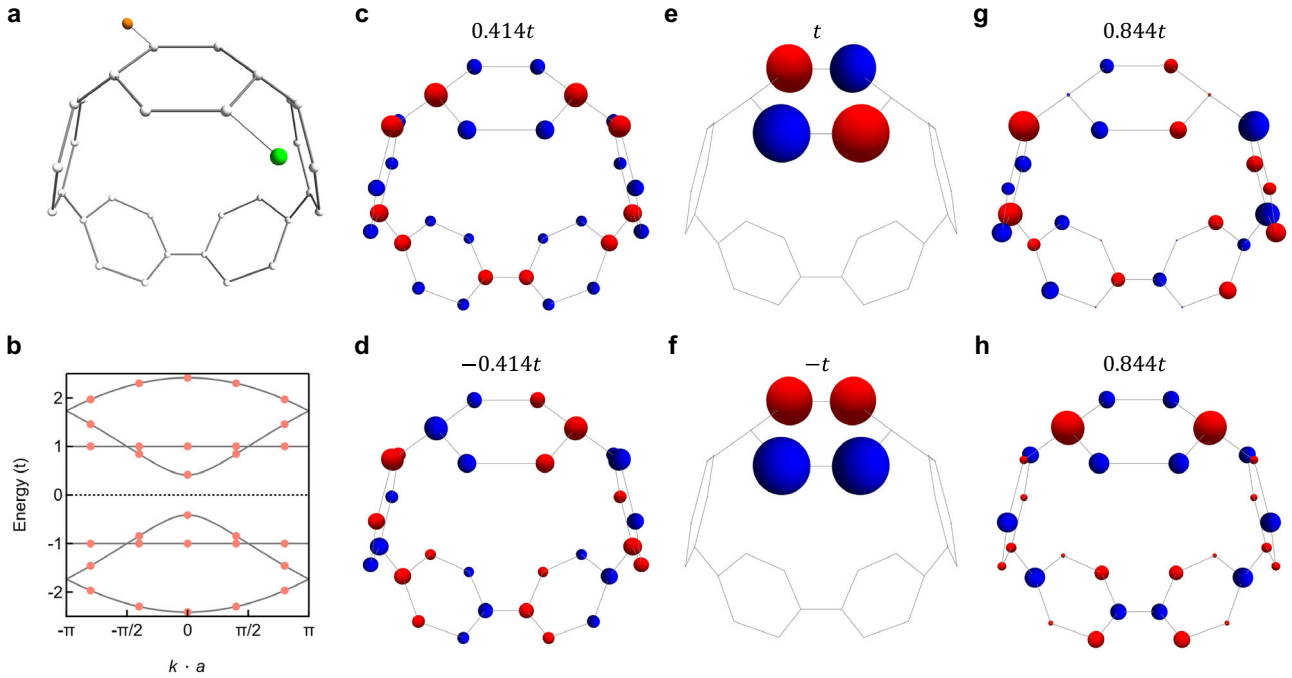

Fig. 1 | Tight-binding orbitals of cycloparaphenylene. a Schematic of a single cycloparaphenylene (CPP) junction with $n = 5$. Gray spheres represent carbon atoms; the green sphere denotes the source electrode, and the orange sphere the drain. **b** Band structure of a [∞]CPP. Pink dots mark the discrete wavevector values that satisfy the cyclic boundary condition for [5]CPP. **c** Real-space amplitude of the lowest unoccupied molecular orbital (LUMO) at energy $0.414t$, where t is the nearest-neighbor hopping integral. **d** Real-space amplitude for the highest occupied molecular orbital (HOMO) at energy $-0.414t$. **e**, **f** Flat band states with energy $\pm t$ with nonzero amplitude on the phenylene ring connected to the electrodes. The other degenerate orbitals at $E = \pm t$ are provided in Supplementary Fig. 1. **g**, **h** Doubly degenerate states at energy $0.844t$, which originate from the $k = \pm 2\pi/5a$ solutions of the conduction band.

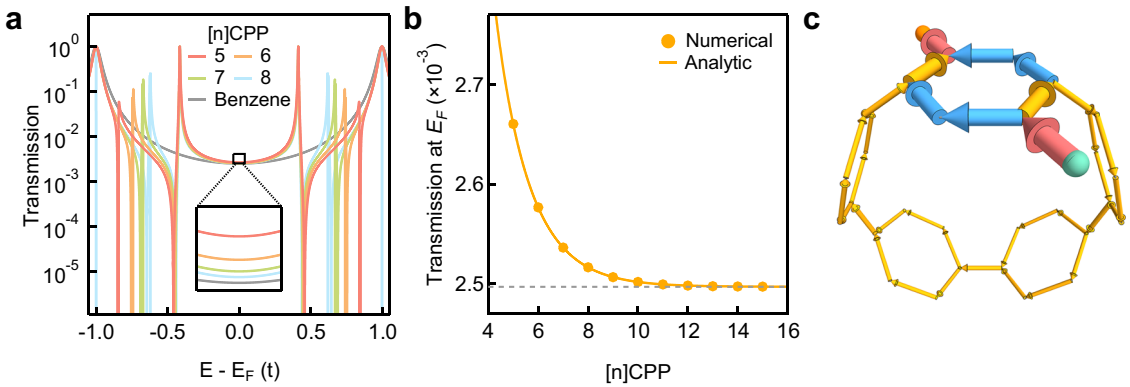

Fig. 2 | Source–drain transmission through cycloparaphenylene junctions. a Energy-dependent source–drain transmission $T(E)$ for [5]CPP, [6]CPP, [7]CPP, and [8]CPP (colored curves) compared with a single-benzene junction (gray). The inset shows the region near the Fermi energy E_F. **b** Transmission at E_F as a function of ring size. The gray dashed line marks the reference value for a single para-connected benzene junction. **c** Energy-resolved local current density maps at E_F for a [5]CPP junction. Arrow widths are scaled with a power-law normalization, $(K_{vw}/K_{\max})^{0.3}$, ensuring small values remain visible while the thickest arrow has the same width in every figure. Here, K_{vw} denotes the energy-resolved local current density from atom w to atom v, and $K_{\max}$ is the maximum magnitude in the corresponding map. Arrows representing source–drain transmission are colored red. Currents that traverse the CPP loop are color-coded by direction: yellow for clockwise (CW) and blue for counter-clockwise (CCW) circulation.

or counter-clockwise ring current is no longer forbidden by symmetry. The transport model used for these contacted junctions is described in "Methods".

Electron transport through a single-molecule junction is captured by the energy-dependent source–drain transmission function. We perform the transmission calculations on CPP junctions following the NEGF formalism described in "Methods". The transmission functions for [n]CPP rings with five to eight phenyl units are presented in Fig. 2a. For comparison, we also calculated a single-benzene junction using the same set of parameters. The transmission spectra of CPP junctions show that resonances at an energy of $E = \pm t$ persist across all sizes, though their narrower widths indicate a weaker coupling between the conducting orbitals and the electrodes than that of a single benzene junction. Moreover, additional resonance peaks appear in the transmission spectra. Specifically, the HOMO and LUMO levels appear as peaks at an energy of $E = \pm\left(\sqrt{2}-1\right)t$, which remains constant regardless of the size of the CPP macrocycle. In contrast, the doubly degenerate resonances shift with the ring size, reflecting the size dependence of their associated wavevectors.

We next focus on the transmission value at the Fermi energy (E_F), which is proportional to the conductance at low bias. As shown in the inset of Fig. 2a and detailed further in Fig. 2b, $T(E_F)$ decreases as the size of the CPP ring increases. Despite this decrease, for finite n, $T(E_F)$ remains higher than that of a single benzene junction. The trend in Fig. 2b suggests that the transmission approaches an asymptotic limit for large rings. To determine this limit, we obtained analytical expressions for $T(E_F)$. For the single benzene junction, the expression is:

$$T_{Benzene}(E_F) = \frac{64\gamma^2 t^2}{\left(\gamma^2 + 16t^2\right)^2} \tag{5}$$

As for the single [n]CPP junction, the expression is (see Supplementary Note 2 and Supplementary Table 1 for details):

$$T_{[n]CPP}(E_F) = \frac{64r^2\gamma^2 t^2}{\left(r^2\gamma^2 + 16t^2\right)^2}, \text{where } r = \frac{2^n}{2^n - 1} \tag{6}$$

By substituting the numerical parameters, we validate the accuracy of the analytical expressions (Fig. 2b). In the limit where n approaches infinity, the ratio factor r goes to 1, and the expression for the [n]CPP junction converges exactly to that of the single benzene junction.

To determine whether the excess transmission of a CPP relative to benzene stems merely from attaching additional phenylene rings on the side of the conductive pathway or instead from the nanohoop's unique closed-loop topology, we "unwrapped" the CPP into its open-chain analog by eliminating the cyclic boundary condition and examined a phenyl unit embedded in linear para-oligophenylenes of increasing length. As detailed in Supplementary Note 3 and Supplementary Fig. 2, $T(E_F)$ remains length independent, indicating that adding phenylene rings in an open geometry does not enhance $T(E_F)$, and the surplus transmission observed in finite CPPs must therefore originate from closing the linear chain into a loop. This finding implies that, besides the direct para pathway, a second channel that threads through the nanohoop contributes to the conductance.

Local currents in cycloparaphenylene

A phenyl ring with a π-conjugated framework usually offers more than one quantum path between the two electrodes. In para-benzene, for instance, an electron can travel through two identical parallel pathways, while larger systems such as the CPPs provide many more paths. However, the transmission function $T(E)$ contains only the total tunneling probability from source to drain. It does not reveal how the current is partitioned among individual paths. To address this shortcoming, we calculate the local current from atoms w to v, I_{vw}, by integrating the energy-resolved local current density[3,30]:

$$I_{vw} = \frac{2e}{h}\int dE\left(f_S(E) - f_D(E)\right)K_{vw}(E) \tag{7}$$

Here, $f_{S,D}(E)$ are the Fermi-Dirac distribution functions of source and drain electrodes, e is the magnitude of the electron charge, h is Planck's constant, and $K_{vw}(E)$ is the local current density from atoms w to v at 0 K. $K_{vw}(E)$ is obtained using the lesser Green's function formalism[3,31,32]. The lesser Green's function implementation is described in "Methods," with the full derivation provided in the Supplementary Method 2. We note that $K_{vw}(E)$ plays the same role in the local current formula as $T(E)$ does in the source–drain current in Landauer–Büttiker formalism[30,33],

$$I_{SD} = \frac{2e}{h}\int dE\left(f_S(E) - f_D(E)\right)T(E) \tag{8}$$

Therefore, the magnitudes of $K_{vw}(E)$ and $T(E)$ can be compared directly. We calculate local current density distribution maps at E_F for the [n]CPP junctions with five to eight phenylene units, $K_{vw}(E_F)$. This map for [5]CPP is shown in Fig. 2c, while the others are shown in Supplementary Fig. 3. For visualization, each $K_{vw}(E)$ element is drawn as an arrow overlayed on the molecular framework. The transmission is represented by arrows that enter the molecule from the source electrode and exit toward the drain electrode. Since this tight-binding model contains only nearest-neighbor couplings, current is restricted to flow through bonds.

The local current density maps clearly show that in addition to the expected direct pathway across the phenylene ring that contacted to electrodes, a distinct macrocyclic pathway exists, which manifests as a ring current circulating around the CPP. This ring current diverges from the main transport path at the ortho-position of the injecting linker atom and rejoins it at the meta-position. The direction of this ring current is dictated by the structural asymmetry of the junction. In other words, coupling the electrodes in this manner induces a specific chirality in the system, which determines the current's circulation. Notably, as shown in Supplementary Fig. 3, the magnitude of this ring current component diminishes as the CPP size increases. This provides a physical explanation for our previous observation: as the CPP macrocycle grows, the influence of the secondary pathway diminishes, and the overall transport becomes increasingly dominated by the phenylene ring directly connected to the electrodes. Consequently, the net transmission converges to the limit of an isolated benzene junction, which lacks the macrocyclic pathway entirely.

We next examine the energy dependence of the ring current density $K_{Ring}(E)$ to understand how an electrostatic gating of the junction could alter the ring currents. Figure 3a shows the net transmission along with the ring component for the [5]CPP junction. To visualize how the current is distributed after injecting into the hoop, we plot local current density maps at the energies marked by black arrows (Fig. 3b–g). The representative energies are all taken from the $E > 0$ side, keeping in mind that the spectra are symmetric about E_F. At the LUMO resonance, $E = \left(\sqrt{2} - 1\right)t$ (Fig. 3b), $K_{Ring}(E)$ is strongly enhanced, reaching a maximum of 0.34, demonstrating that roughly a third of the current carried by the frontier orbital circulates around the hoop rather than flowing solely across the phenylene connected to the leads. By contrast, the ring current vanishes at $E = +t$ (Fig. 3g). The orbital at this energy is strongly localized on the phenylene directly attached to the electrodes, leading to a broad resonance peak in the net transmission but contributing no circulating component around the macrocycle.

Distinctive behavior emerges near doubly degenerate resonances, which originate from the paired states with wavevectors $+k$ and $-k$ both satisfying the cyclic boundary condition as discussed above. For instance, at $E \approx 0.843 - 0.844t$ (Fig. 3e, f), within a very narrow energy window around this resonance pair, destructive interference causes an abrupt change of the local current pattern and reversal of the ring current direction. We discuss the origin of such abrupt energy-dependent ring current reversal in the Supplementary Method 2. Beyond these resonances, the relative weight of the ring pathway varies with energy. $K_{Ring}(E)$ can exceed, fall below, or equal $T(E)$. Two examples occur at $E \approx 0.443t$ and $E \approx 0.780t$ (Fig. 3c, d), where current is exclusively through the CPP ring while the contact phenylene is bypassed, with clockwise (CW) circulation at the former and counter clockwise (CCW) at the latter.

https://doi.org/10.1038/s41467-026-74365-6

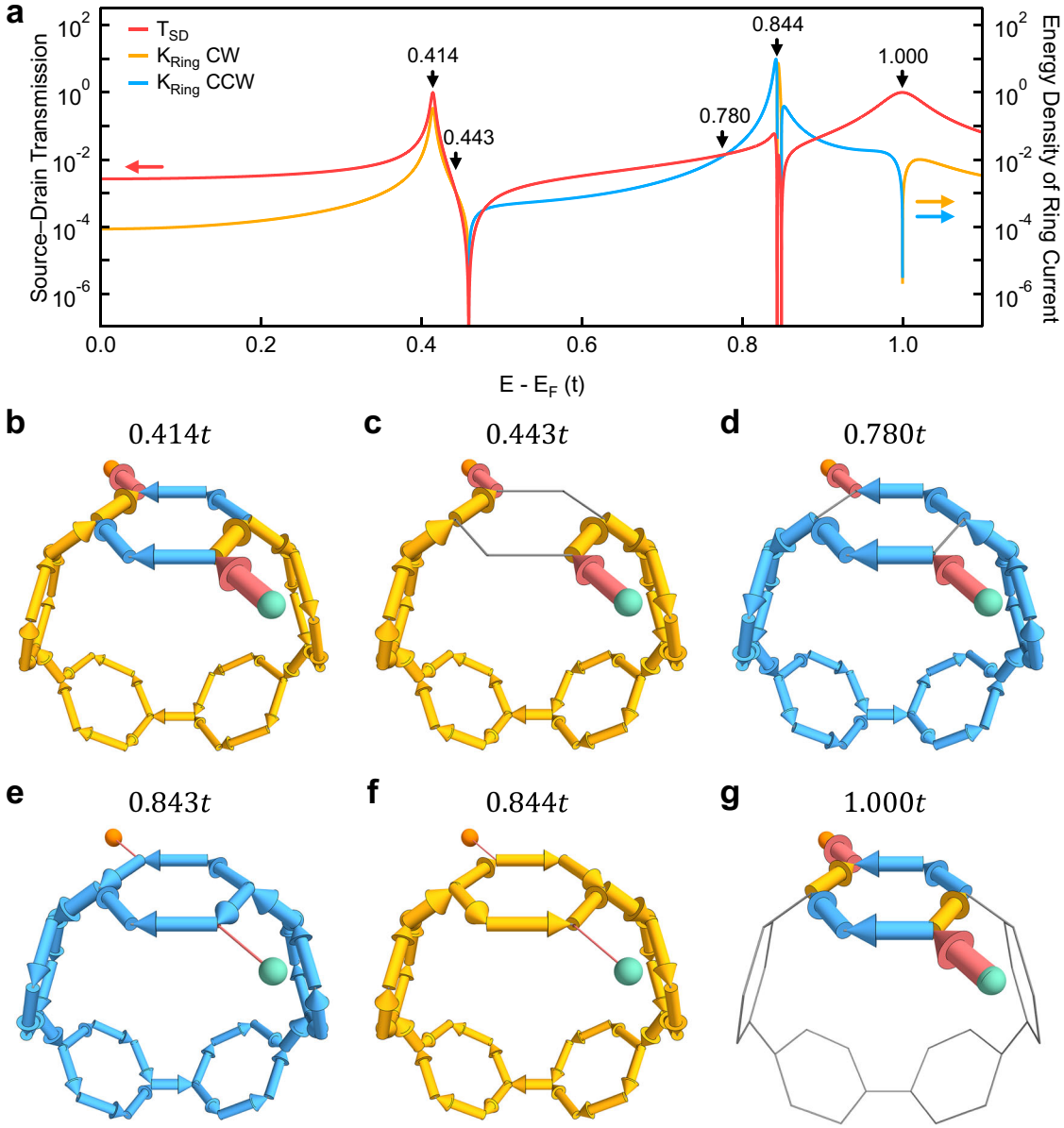

Fig. 3 | Energy-dependent local current density maps of [5]CPP junction. **a** Energy-dependent transmission function (red) and ring current density circulating the [5]CPP cycle. The ring current can circulate clockwise (CW, yellow) or counter-clockwise (CCW, blue), depending on energy. Black arrows label the energy positions of the corresponding local current density maps. **b**–**g** Local current density maps for [5]CPP junctions at different energies indicated.

Atomistic currents in a gold cycloparaphenylene junction

While the tight-binding model represents a minimal model that effectively captures the transport trends and provides a detailed understanding of the underlying mechanisms, it is a vast simplification. Unless an ab-initio-based parametrization is used, its results cannot quantitatively be compared with experiments: generic tight-binding calculations use a very simple basis, which only includes one single p_z orbital per carbon atom and only considers nearest-neighbor hopping. Consequently, it neglects the contributions of other orbitals, structural distortions, and long-range electronic couplings. To overcome these limitations, we now turn to ab initio transport calculations. Unlike the tight-binding model, a DFT Hamiltonian accounts for the orbital hybridization and long-range interactions specific of a given molecule that are critical in radially conjugated, highly curved CPPs. We carried out the transport calculations for the Au–CPP–Au junction shown in Fig. 4a within the NEGF framework. The workflow is described in "Methods".

As shown in Fig. 4b, the DFT transmission spectrum validates the basic features we observed in the tight-binding model while introducing the complexity characteristic of a realistic junction. In the off-resonant regime near E_F, transport is predominantly driven by the HOMO resonance. Such hole-type transport is a typical feature of Au-contacted π-conjugated systems. We observe the HOMO and LUMO resonances as singly degenerate peaks positioned at −0.28 eV and 2.16 eV. At energies further away from E_F, some resonances tend to group into quasi-degenerate pairs. If the CPP were idealized and highly symmetric, these states would be degenerate. In DFT, the cyclic symmetry is lifted. Both the inter-phenylene structural distortions and the strong coupling to the electrodes contribute to this effect, broadening and splitting the degenerate energy levels.

Since the DFT Hamiltonian includes multi-orbital basis sets and long-range couplings, current flow is not strictly confined through bonds that link adjacent atoms. Instead, the local current distributes across a complex network that includes non-nearest-neighbor

https://doi.org/10.1038/s41467-026-74365-6

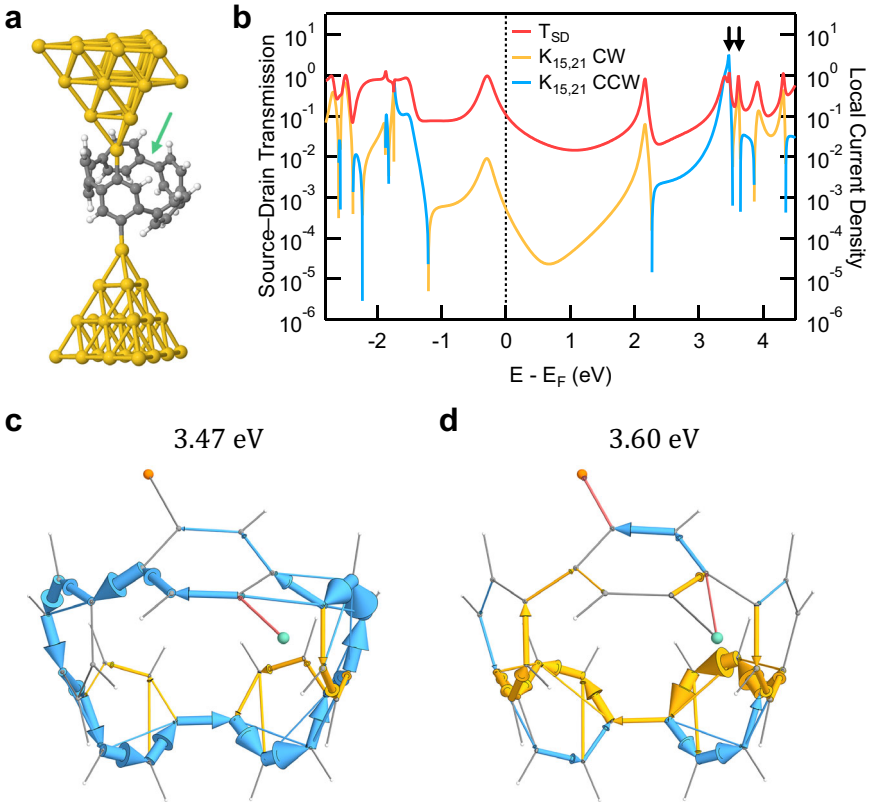

Fig. 4 | DFT local currents in a gold [5]CPP junction. a Geometry of the Au_{22}-[5]CPP-Au_{22} junction used for density functional theory (DFT) calculations. The green arrow marks the bond between atom 15 and 21 used to monitor the circulating component. **b** Energy-dependent source–drain transmission and the local current density component $K_{15,21}$ across the highlighted bond. The red curve shows the source–drain transmission T_{SD} on the left axis. The yellow and blue curves show the magnitude of $K_{15,21}$ on the right axis for clockwise (CW) and counter-clockwise (CCW) circulation around the [5]CPP macrocycle, respectively. Black arrows label the energies used for the local current density maps in (**c**, **d**). **c**, **d** Local current density maps at the energies marked in (**b**). For clarity, only the two Au atoms bonded to the [5]CPP are shown in green and orange, indicating the source and drain Au atoms, and components smaller than 10% of the maximum are omitted. Note that charge conservation is strictly satisfied, and any apparent current imbalance is a visualization artifact of this 10% cutoff (see Supplementary Fig. 4 for the complete 0% threshold maps).

pathways. To quantitatively evaluate the circulating current component within this network, we extracted the local current element $K_{15,21}(E)$ across the C15–C21 bond (as indicated by the green arrow in Fig. 4a) as a representative probe. Figure 4b shows $K_{15,21}(E)$, which changes sign as a function of energy when crossing resonances, confirming the reversal of the ring current direction predicted by the tight-binding calculation. Near the quasi-degenerate states around 3.47 eV, the magnitude $|K_{15,21}(E)|$ exceeds the total source-drain transmission $T_{SD}(E)$, confirming that quantum interference can strongly amplify circulating currents. To visualize this effect, we plot the local current density maps at two representative energies with amplified circulating currents, $E = 3.47$ eV and 3.60 eV (Fig. 4c, d). For clarity, current components below 10% of the maximum component magnitude in the corresponding map, and the bulk Au electrode atoms (except for the adatoms) are omitted. We emphasize that strict charge conservation is satisfied in the calculations, and the current imbalance in Fig. 4c, d is just a visualization artifact arising from this 10% threshold. The complete current networks plotted with a 0% threshold, along with maps at the HOMO and LUMO resonances, are provided in Supplementary Fig. 4. These maps reveal that there are persistent ring currents flowing around the entire macrocycle. Furthermore, the DFT calculated maps clearly show localized current vortices within individual phenylene units, alongside distinct non-nearest-neighbor current components. The localized loops arise naturally from the complex intra-ring quantum interference enabled by the full orbital basis and long-range electronic couplings. We can conclude that ring current signatures are also clearly seen in the ab initio Au–CPP–Au junction.

To quantify how the electrostatic gating can modulate the local current distribution and magnetic field in a single CPP junction, we convert the $K(E)$ into a gate voltage (V_{Gate}) dependent local current network by integrating the Landauer-type formulas Eqs. (7) and (8) given above. A fixed experimentally relevant bias voltage of 100 mV was applied symmetrically between the two electrodes. V_{Gate} is included as a shift of the electrochemical potential in the Fermi-Dirac functions, i.e., $f_{S,D}(E - eV_{Gate})$. In practice, gating the junction across a molecular resonance may alter the transmission, particularly if the single-particle model breaks down because of charging, image-charge effects, electron–electron interactions, and electron–vibrational coupling[34,35]. Within an interacting Green's-function description, these effects enter through self-energy corrections that can shift and broaden molecule-derived spectral features[36,37]. The phase structure of the corresponding matrix elements/residues, which determines constructive or destructive interference between transport channels, is expected to change more smoothly unless the relevant molecular symmetry or orbital ordering is modified. We therefore expect these effects to shift the gate voltage at which the enhancement occurs and to renormalize the absolute current and magnetic-field magnitude, rather than eliminate the circulating current or the field reversal. The near-resonant fields should thus be regarded as coherent-transport estimates for the design of single-molecule electromagnets. Notably, coherent many-body transport in gated molecular devices is well established, as evidenced by phenomena such as the Kondo effect[38,39]. A quantitative

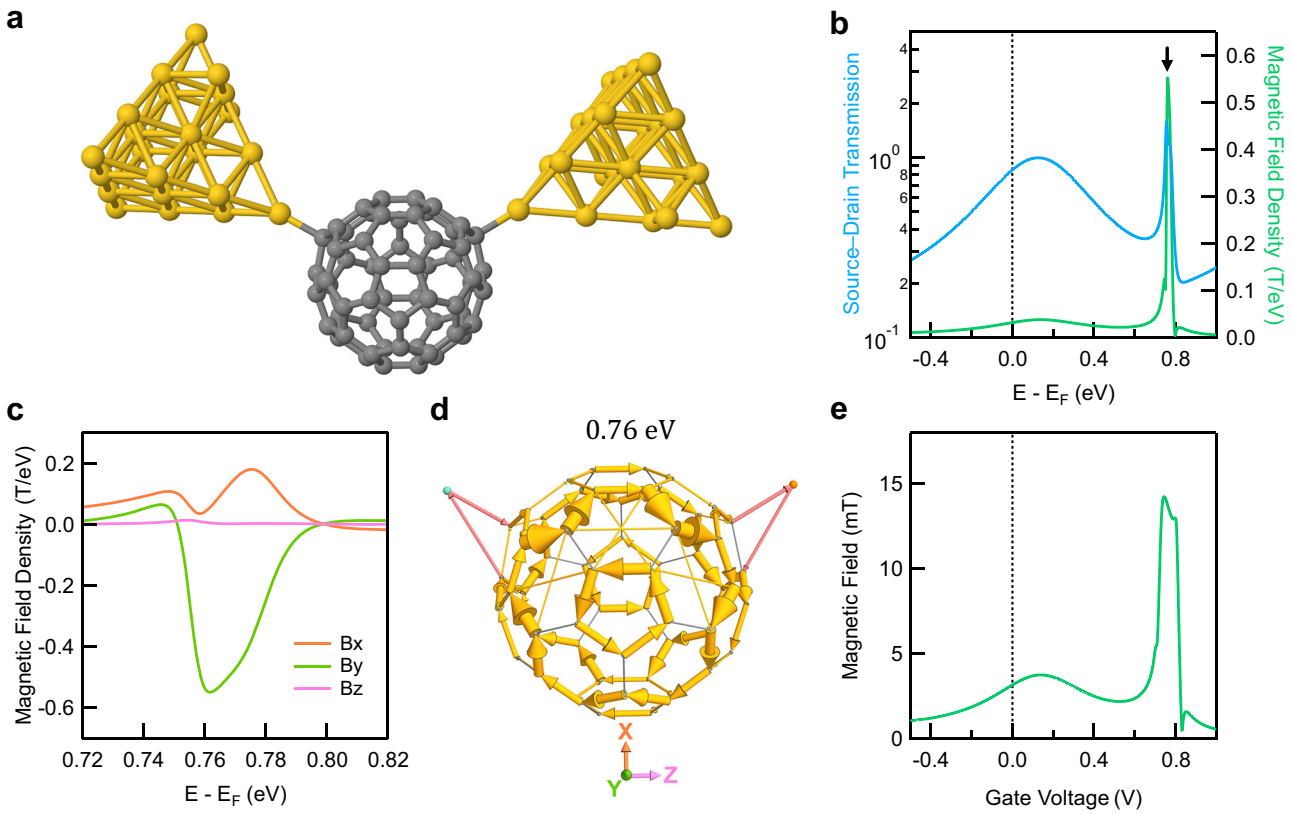

Fig. 5 | Magnetic field response in a gold fullerene junction. a Geometry of the Au–C_{60}–Au junction used for the calculations, where the electrodes are coupled across the C_{60} molecule to induce chirality. **b** Energy-dependent source–drain transmission together with the induced energy-resolved magnetic field density. Black arrow marks the energy used for the local current density maps in (**d**). **c** Three Cartesian components of the induced energy-resolved magnetic field density. **d** DFT local current density map at $E = 0.76$ eV, showing multiple local current vortices distributed across the fullerene cage. **e** Calculated magnetic-field magnitude as a function of gate voltage under a constant 100 mV source–drain bias at 0 K.

treatment of this regime would require explicit interacting nonequilibrium approaches, such as nonequilibrium dynamical mean-field theory[40], which are beyond the scope of the present atomistic DFT-NEGF/AITRANSS workflow.

The gate-tunable axial magnetic fields in a single [5]CPP junction under 0 K and 300 K are shown in Supplementary Fig. 5. These calculations show that, in principle, the axial magnetic field could be boosted as large as 21 mT when E_F is gated to the nearly doubly degenerate resonances around 3.47 eV. However, such an electrostatic gating condition could be difficult to achieve experimentally, since the effective gate coupling is often limited by electrostatic screening from the source and drain electrodes[41,42].

Magnetic fields in a gold fullerene junction

To validate whether our design principles extend to a radially π-conjugated molecule with a more accessible gating window, we perform calculations for an Au–C_{60}–Au single-molecule junction, as shown in Fig. 5. Single-molecule C_{60} devices provide a relevant computational test case here, because charge transport through such junctions has been measured experimentally and gate-controlled charge states have already been demonstrated in single-C_{60} transistor devices[23–25].

The single-C_{60} junction geometry we considered is shown in Fig. 5a, and the corresponding source–drain transmission together with the induced energy-resolved magnetic field density are shown in Fig. 5b. In the junction, the LUMO resonance appears at ~0.1 eV above E_F, well within an energy range closer to those accessed in gated single-molecule devices than the higher-energy CPP resonances considered above. The magnetic field is enhanced near this resonance but not very strongly, because the LUMO resonance is non-degenerate. In contrast, at the higher-lying degenerate resonances around 0.76 eV, the magnetic field strength is amplified by quantum interference between the degenerate channels, yielding a ~15-fold enhancement relative to the LUMO peak, which is fully consistent with the mechanism established using CPPs as prototypes.

Because C_{60} is a closed cage rather than a planar ring like the CPPs, it does not have a unique ring plane that could be used to define a physically meaningful normal magnetic field component. Accordingly, for C_{60}, we analyze the full vector magnetic-field response rather than assigning a single axial component. We therefore plot the three Cartesian components separately in Fig. 5c, which reveals a rapid orientation switch of the induced field within a narrow energy window of ~0.01 eV. In Fig. 5d, the DFT-computed local current density map at 0.76 eV exhibits multiple local current vortices distributed across the cage, generating the enhanced magnetic field. Figure 5e shows the magnetic field under a constant 100 mV source–drain bias and gate voltage sweep at 0 K. Given the low-lying LUMO resonance, the calculated magnetic field at E_F is around 3.1 mT. As the gate voltage approaches the LUMO resonance, the magnetic field is enhanced to 3.7 mT. After reaching the degenerate resonances around 0.76 eV, the magnetic field reaches 14.2 mT. This field is notably stronger than a common refrigerator magnet (~5 mT)[2]. Compared with the CPP junction, the key advantage of fullerene is therefore not a qualitatively different mechanism, but a lower-energy window for the same calculated interference-driven enhancement. In this sense, the Au–C_{60}–Au calculation provides a test case for the design principles established above.

Discussion

In conclusion, we demonstrate the potential of utilizing radially π-conjugated carbon structures as design platforms for effective single-molecule electromagnets. Using CPP junctions as prototypical systems, we show that bias-driven transport can contain a substantial circulating component in addition to the direct source–drain pathway. Tight-binding, NEGF, and local current calculations show the ring current is dependent on loop size and the electrostatic gate. NEGF-DFT calculations on an Au-[5]CPP-Au junction confirm that this ring current persists beyond the idealized and simplified tight-binding model. We further show that the same interference-driven design principle also applies to Au–C_{60}–Au junctions, whose lower-lying degenerate resonances make the calculated enhancement less demanding in gate energy than in CPPs. By evaluating the magnetic field at the C_{60} geometric center using the Biot–Savart law, we obtain gate-tunable fields that reach up to 14.2 mT under a 100 mV bias. These findings unveil the potential of radially π-conjugated carbon structures as electronically tunable, atomically precise sources of nanoscale magnetic flux and provide a simple method for designing single-molecule devices with inductive functionality.

Methods

Molecular junction model

Source and drain electrodes were incorporated through non-Hermitian self-energies, giving the open system Hamiltonian:

$$\mathbf{H}_{Junction} = \mathbf{H}_{Isolate} + \Sigma_S + \Sigma_D \tag{9}$$

where Σ_S and Σ_D are the self-energy terms of source and drain electrodes, respectively. The electrode coupling matrices were defined by the anti-Hermitian part of the self-energies,

$$\Gamma_{S,D} = i\left(\Sigma_{S,D} - \Sigma_{S,D}^{\dagger}\right) = -2\mathrm{Im}\left[\Sigma_{S,D}\right] \tag{10}$$

For the tight-binding calculations, the couplings were treated as energy independent in the wide-band limit. Each electrode was coupled to a single p_z orbital on the contacted linker atom, so the source and drain coupling matrices were rank-one projectors. The coupling strengths were set to $\gamma = 0.1t$, giving symmetrically and weakly coupled junctions.

Junction transmission

The retarded Green's function was calculated as:

$$G(E) = \left[EI - \mathbf{H}_{Junction}\right]^{-1} = \left[EI - \mathbf{H}_{Isolate} + \frac{i\left(\Gamma_S + \Gamma_D\right)}{2}\right]^{-1} \tag{11}$$

The source–drain transmission was then evaluated within the Landauer–Büttiker formalism as:

$$T(E) = Tr\left[\Gamma_S G \Gamma_D G^{\dagger}\right] \tag{12}$$

The same coupling convention was used for benzene, [n]CPP, and para-oligophenylene junctions. Analytical expressions for $T(E_F)$ were obtained by keeping t and γ symbolic in Mathematica. The full coefficient table and simplification are provided in the Supplementary Note 2 and Supplementary Table 1.

Local current density

The energy-resolved local current density from atom w to atom v was evaluated with the lesser Green's function formalism as

$$K_{vw}(E) = 2\mathbf{H}_{vw}\mathrm{Im}\left[\left(\mathrm{G(E)}\Gamma_S\mathrm{G}^{\dagger}\mathrm{(E)}\right)_{vw}\right] \tag{13}$$

Full derivation details are provided in the Supplementary Method 2. For the nearest-neighbor tight-binding Hamiltonian, non-zero local current elements are distributed only on adjacent carbon-carbon bonds. Ring-current densities were extracted from the $K_{vw}(E)$ elements that traverse the CPP macrocycle. In the current-density maps, each element is drawn as an arrow on the molecular framework.

First principles transport calculations

The ab initio DFT-based calculations were carried out using the FHI-aims and AITRANSS packages[43–48]. We employed the B3LYP hybrid exchange-correlation functional and accounted for scalar relativistic corrections to the kinetic energy at the atomic zeroth-order regular approximation level[49–52]. The calculations utilized standard "light" numeric atom-centered orbital basis sets with the "first tier" of additional basis functions enabled. Specifically, the basis set for Au comprised the minimal valence functions (6s, 5p, 5d, 4f) augmented by the active first-tier functions (ionic 6s, 6p, and hydrogenic 3d, 4f). For C, the minimal basis (2s, 2p) was augmented by hydrogenic 2s, 2p, and 3d functions. For H, the minimal basis (1s) was augmented by hydrogenic 2s and 2p functions.

We initially relax the geometry of a molecule coupled to a single Au atom on both sides. Following this optimization, each Au atom was expanded into a 4-layer Au_{22} pyramid to model the electrode, as shown in Fig. 4a in the manuscript. For all subsequent transport calculations, the junction geometry was kept frozen without any further structural relaxation.

In AITRANSS, each junction was partitioned into source and drain electrodes and an extended molecule. Electrode coupling was included through energy-dependent self-energies, and the resulting non-Hermitian effective Hamiltonian was diagonalized to obtain complex poles and biorthogonal eigenvectors. The source-injected density matrix was reconstructed (see Supplementary Method 3) as $\rho(E) = G(E)\Gamma_S(E)G^{\dagger}(E)$. The atomic orbital resolved local current density matrix was then calculated as

$$K_{\mu\nu}^{\mathrm{AO}}(E) = 2H_{\mu\nu}^{\mathrm{AO}}\mathrm{Im}\left[\rho_{\mu\nu}(E)\right] \tag{14}$$

The orbital resolved matrix was aggregated into an atom-resolved matrix according to

$$K_{vw}^{\mathrm{atom}}(E) = \sum_{\mu\in v}\sum_{\nu\in w} K_{\mu\nu}^{\mathrm{AO}}(E) \tag{15}$$

Here, μ and ν run over atomic orbitals on atoms v and w, respectively. Finite bias atom-to-atom local currents were obtained by integrating $K_{vw}^{\mathrm{atom}}(E)$ with the Fermi-Dirac distribution as in Eq. (7). Unlike in the nearest-neighbor tight-binding model, the DFT-based Hamiltonian contains a multi-orbital basis and long-range couplings, so the resulting local current network is not restricted to adjacent bonds.

Magnetic field calculation

The atom-resolved local current matrix was converted into a three-dimensional spatial current network using the optimized atomic coordinates. For CPP and C_{60}, the observation point was the geometric center of the carbon backbone. Before applying the Biot–Savart summation, all atomic coordinates were translated so that the selected observation point was at the origin. For a current element from atom w to atom v, the element position was defined as $\vec{r}_{\mathrm{mid}} = (\vec{r}_v + \vec{r}_w)/2$. The magnetic field at the selected observation point was evaluated with the discretized Biot–Savart summation:

$$\vec{B} = \frac{\mu_0}{4\pi}\sum_{v,w} I_{vw}\frac{\vec{r}_w \times \vec{r}_v}{|\vec{r}_{\mathrm{mid}}|^3} \tag{16}$$

Here, I_{vw} is the finite-bias current from atom w to atom v, and μ_0 is the vacuum permeability. Current pathways involving Au electrode atoms were excluded from the summation to isolate the molecular response.

The CPP plane was determined by principal component analysis of the carbon positions, and the axial field was obtained by projecting $\vec{B}$ onto the corresponding normal vector. For C_{60}, the three Cartesian field components and the field magnitude were evaluated instead of assigning a single axial component.

Data availability

The data generated in this study have been deposited in the Code Ocean capsule. The capsule contains the FHI-aims and AITRANSS output matrices used for post-processing, precomputed cache files, and optimized atomic coordinate files. These data are sufficient to reproduce the results reported in the paper.

Code availability

The code used to reproduce the local-current and magnetic-field analyses is available in the Code Ocean capsule. The capsule includes Python scripts for post-processing DFT output matrices and Mathematica notebooks for tight-binding calculations and reproducing visualizations.

References

1. Rai, D., Hod, O. & Nitzan, A. Magnetic fields effects on the electronic conduction properties of molecular ring structures. *Phys. Rev. B Condens. Matter Mater. Phys.* **85**, 155440 (2012).
2. Bro-Jørgensen, W., Sauer, S. P. A., Solomon, G. C. & Garner, M. H. Substantial magnetic fields arising from ballistic ring currents in single-molecule junctions. *JACS Au* **5**, 4073–4085 (2025).
3. Solomon, G. C., Herrmann, C., Hansen, T., Mujica, V. & Ratner, M. A. Exploring local currents in molecular junctions. *Nat. Chem.* **2**, 223–228 (2010).
4. Rai, D., Hod, O. & Nitzan, A. Circular currents in molecular wires. *J. Phys. Chem. C.* **114**, 20583–20594 (2010).
5. Walz, M., Wilhelm, J. & Evers, F. Current patterns and orbital magnetism in mesoscopic dc transport. *Phys. Rev. Lett.* **113**, 136602 (2014).
6. Tahara, K. & Tobe, Y. Molecular loops and belts. *Chem. Rev.* **106**, 5274–5290 (2006).
7. Jasti, R., Bhattacharjee, J., Neaton, J. B. & Bertozzi, C. R. Synthesis, characterization, and theory of [9]-, [12]-, and [18]cycloparaphenylene: carbon nanohoop structures. *J. Am. Chem. Soc.* **130**, 17646–17647 (2008).
8. Takaba, H., Omachi, H., Yamamoto, Y., Bouffard, J. & Itami, K. Selective synthesis of [12]cycloparaphenylene. *Angew. Chem. Int. Ed.* **48**, 6112–6116 (2009).
9. Yamago, S., Watanabe, Y. & Iwamoto, T. Synthesis of [8]cycloparaphenylene from a square-shaped tetranuclear platinum complex. *Angew. Chem. Int. Ed.* **49**, 757–759 (2010).
10. Omachi, H., Matsuura, S., Segawa, Y. & Itami, K. A modular and size-selective synthesis of [n]cycloparaphenylenes: a step toward the selective synthesis of [n,n] single-walled carbon nanotubes. *Angew. Chem. Int. Ed.* **49**, 10202–10205 (2010).
11. Iwamoto, T., Watanabe, Y., Sakamoto, Y., Suzuki, T. & Yamago, S. Selective and random syntheses of [n]cycloparaphenylenes (n=8–13) and size dependence of their electronic properties. *J. Am. Chem. Soc.* **133**, 8354–8361 (2011).
12. Darzi, E. R., Sisto, T. J. & Jasti, R. Selective syntheses of [7]-[12] cycloparaphenylenes using orthogonal Suzuki-Miyaura cross-coupling reactions. *J. Org. Chem.* **77**, 6624–6628 (2012).
13. Segawa, Y. et al. Concise synthesis and crystal structure of [12] cycloparaphenylene. *Angew. Chem. Int. Ed.* **50**, 3244–3248 (2011).
14. Xia, J., Bacon, J. W. & Jasti, R. Gram-scale synthesis and crystal structures of [8]- and [10]cpp, and the solid-state structure of C_{60}@[10]CPP. *Chem. Sci.* **3**, 3018–3021 (2012).
15. Leonhardt, E. J. & Jasti, R. Emerging applications of carbon nanohoops. *Nat. Rev. Chem.* **3**, 672–686 (2019).
16. Ozaki, N. et al. Electrically activated conductivity and white light emission of a hydrocarbon nanoring-iodine assembly. *Angew. Chem. Int. Ed.* **56**, 11196–11202 (2017).
17. Kayahara, E., Fukayama, K., Nishinaga, T. & Yamago, S. Size dependence of [n]cycloparaphenylenes (n=5-12) in electrochemical oxidation. *Chem. Asian J.* **11**, 1793–1797 (2016).
18. Yang, S., Pettiette, C. L., Conceicao, J., Cheshnovsky, O. & Smalley, R. Ups of buckminsterfullerene and other large clusters of carbon. *Chem. Phys. Lett.* **139**, 233–238 (1987).
19. Huang, D.-L., Dau, P. D., Liu, H.-T. & Wang, L.-S. High-resolution photoelectron imaging of cold C_{60}^- anions and accurate determination of the electron affinity of C_{60}. *J. Chem. Phys.* **140**, 224315 (2014).
20. Lv, Y. et al. Single cycloparaphenylene molecule devices: Achieving large conductance modulation via tuning radial pi-conjugation. *Sci. Adv.* **7**, eabk3095 (2021).
21. Lin, J. et al. Cleavage of non-polar c(sp(2))–c(sp(2)) bonds in cycloparaphenylenes via electric field-catalyzed electrophilic aromatic substitution. *Nat. Commun.* **14**, 293 (2023).
22. Hu, L. Z., Guo, Y. D., Yan, X. H., Zeng, H. L. & Zhou, J. Electronic transport properties in [n]cycloparaphenylenes molecular devices. *Phys. Lett. A* **381**, 2107–2111 (2017).
23. Böhler, T., Edtbauer, A. & Scheer, E. Conductance of individual c 60 molecules measured with controllable gold electrodes. *Phys. Rev. B Condens. Matter Mater. Phys.* **76**, 125432 (2007).
24. Evangeli, C. et al. Engineering the thermopower of C_{60} molecular junctions. *Nano Lett.* **13**, 2141–2145 (2013).
25. Park, H. et al. Nanomechanical oscillations in a single-C_{60} transistor. *Nature* **407**, 57–60 (2000).
26. Gehring, P., Thijssen, J. M. & van der Zant, H. S. J. Single-molecule quantum-transport phenomena in break junctions. *Nat. Rev. Phys.* **1**, 381–396 (2019).
27. Segawa, Y. et al. Combined experimental and theoretical studies on the photophysical properties of cycloparaphenylenes. *Org. Biomol. Chem.* **10**, 5979–5984 (2012).
28. Golder, M. R. & Jasti, R. Syntheses of the smallest carbon nanohoops and the emergence of unique physical phenomena. *Acc. Chem. Res.* **48**, 557–566 (2015).
29. Alvarez, M. P. et al. Properties of sizeable [n]cycloparaphenylenes as molecular models of single-wall carbon nanotubes elucidated by raman spectroscopy: Structural and electron-transfer responses under mechanical stress. *Angew. Chem. Int. Ed.* **53**, 7033–7037 (2014).
30. Datta, S. *Electronic Transport in Mesoscopic Systems*. (Cambridge University Press, 1997).
31. Todorov, T. N. Tight-binding simulation of current-carrying nanostructures. *J. Phys. Cond. Matter* **14**, 3049–3084 (2002).
32. Pecchia, A. & Di Carlo, A. Atomistic theory of transport in organic and inorganic nanostructures. *Rep. Prog. Phys.* **67**, 1497–1561 (2004).
33. Buttiker, M., Imry, Y., Landauer, R. & Pinhas, S. Generalized many-channel conductance formula with application to small rings. *Phys. Rev. B* **31**, 6207–6215 (1985).
34. Galperin, M., Ratner, M. A., Nitzan, A. & Troisi, A. Nuclear coupling and polarization in molecular transport junctions: beyond tunneling to function. *Science* **319**, 1056–1060 (2008).
35. Neaton, J. B., Hybertsen, M. S. & Louie, S. G. Renormalization of molecular electronic levels at metal-molecule interfaces. *Phys. Rev. Lett.* **97**, 216405 (2006).

36. Meir, Y. & Wingreen, N. S. Landauer formula for the current through an interacting electron region. *Phys. Rev. Lett.* **68**, 2512 (1992).
37. Jauho, A.-P., Wingreen, N. S. & Meir, Y. Time-dependent transport in interacting and noninteracting resonant-tunneling systems. *Phys. Rev. B* **50**, 5528 (1994).
38. Mitchell, A. K., Pedersen, K. G., Hedegård, P. & Paaske, J. Kondo blockade due to quantum interference in single-molecule junctions. *Nat. Commun.* **8**, 15210 (2017).
39. Liang, W., Shores, M. P., Bockrath, M., Long, J. R. & Park, H. Kondo resonance in a single-molecule transistor. *Nature* **417**, 725–729 (2002).
40. Aoki, H. et al. Nonequilibrium dynamical mean-field theory and its applications. *Rev. Mod. Phys.* **86**, 779–837 (2014).
41. Song, H. et al. Observation of molecular orbital gating. *Nature* **462**, 1039–1043 (2009).
42. Datta, S. S., Strachan, D. R. & Johnson, A. C. Gate coupling to nanoscale electronics. *Phys. Rev. B Condens. Matter Mater. Phys.* **79**, 205404 (2009).
43. Blum, V. et al. Molecular simulations with numeric atom-centered orbitals. *Comp. Phys. Commun.* **180**, 2175–2196 (2009).
44. Arnold, A., Weigend, F. & Evers, F. Quantum chemistry calculations for molecules coupled to reservoirs: formalism, implementation, and application to benzenedithiol. *J. Chem. Phys.* **126**, 174101 (2007).
45. Ren, X. G. et al. Resolution-of-identity approach to Hartree-Fock, hybrid density functionals, RPA, MP2 and GW with numeric atom-centered orbital basis functions. *New J. Phys.* **14**, 053020 (2012).
46. Wilhelm, J., Walz, M., Stendel, M., Bagrets, A. & Evers, F. Ab initio simulations of scanning-tunneling-microscope images with embedding techniques and application to C_{58}-dimers on Au (111). *Phys. Chem. Chem. Phys.* **15**, 6684–6690 (2013).
47. Camarasa-Gómez, M., Hernangómez-Pérez, D., Wilhelm, J., Bagrets, A. & Evers, F. Molecular transport. Preprint at *arXiv* https://doi.org/10.48550/arXiv.2411.01680 (2024).
48. Camarasa-Gómez, M., Hernangómez-Pérez, D. & Evers, F. Spin–orbit torque in single-molecule junctions from ab initio. *J. Phys. Chem. Lett.* **15**, 5747–5753 (2024).
49. Lenthe, E. V., Baerends, E.-J. & Snijders, J. G. Relativistic regular two-component hamiltonians. *J. Chem. Phys.* **99**, 4597–4610 (1993).
50. Becke, A. D. Density-functional thermochemistry. III. The role of exact exchange. *J. Chem. Phys.* **98**, 5648–5652 (1993).
51. Vosko, S. H., Wilk, L. & Nusair, M. Accurate spin-dependent electron liquid correlation energies for local spin density calculations: a critical analysis. *Can. J. Phys.* **58**, 1200–1211 (1980).
52. Scuseria, G. E. Recent progress in the development of exchange-correlation functionals. *Abstr. Pap. Am. Chem. Soc.* **229**, U763–U763 (2005).

Acknowledgements

The authors thank Jascha Repp from the University of Regensburg for helpful discussions. This paper is dedicated to the memory of Prof. Mark Ratner in appreciation of the encouragement offered many years ago, and whose influence had endured ever since.

Author contributions

W.S. and L.V. conceived the idea and developed this work. W.S. performed calculations and analyzed the results. R.K. and F.E. contributed to discussions relating to the calculations, while J.D.T. contributed to discussions of cycloparaphenylene chemistry. L.V. supervised the project. W.S. and L.V. wrote the manuscript with input from all authors.

Funding

This work was supported by the National Science Foundation under grant NSF-DMR 2241180 and the Institute of Science and Technology Austria. The collaboration between L.V., R.K., and F.E. was supported by the Humboldt Foundation. This research was funded in part by the Austrian Science Fund (FWF) [10.55776/COE5] (Cluster of Excellence MECS).

Competing interests

The authors declare no competing interests.

Additional information

Supplementary information The online version contains supplementary material available at https://doi.org/10.1038/s41467-026-74365-6.

Correspondence and requests for materials should be addressed to Latha Venkataraman.

Peer review information *Nature Communications* thanks the anonymous reviewer(s) for their contribution to the peer review of this work. A peer review file is available.